CrossMark

Online prediction model for wheel wear considering track flexibility

Gongquan Tao[1] · **Dexiang Ren[1]** · **Linfeng Wang[2]** ·
Zefeng Wen[1] · **Xuesong Jin[1]**

Abstract The objective of this study is to develop a new online model for wheel wear that takes into account the track flexibility. The proposed model consists of two parts that interact with each other, namely, (a) a locomotive/track coupled dynamics model considering the track flexibility, which is validated by field measurement results, and (b) a model for the wear estimation. The wheel wear prediction model can be employed in online solutions rather than in post-processing. The effect of including the track flexibility on the wear estimation is investigated by comparing the results with those obtained for a rigid track. Moreover, the effect of the wheel profile updating strategy on the wheel wear is also examined. The simulation results indicate that the track flexibility cannot be neglected for the wheel wear prediction. The wear predicted with the rigid track model is generally larger than that predicted with the flexible track model. The strategy of maintaining unchanged wheel profiles during the dynamic simulation coincides with the online updating strategy in terms of the predicted wear.

Keywords Electric locomotive · Wheel wear · Track flexibility · Online simulation

1 Introduction

Wheel/rail wear, which can modify the wheel/rail profile, is an important problem in the railway industry. The evolution of the wheel/rail wear profile can deteriorate the vehicle/track dynamic performance. To ensure a consistent dynamic behavior and safety of a train during operation, the wear profiles must be periodically re-profiled by turning the wheels or grinding the rails. However, the method to determine or optimize the maintenance interval, which has a significant effect on the lifetime of the wheels and rails and maintenance costs, is a key

✉ Z. Wen
zfwen@home.swjtu.edu.cn

[1] State Key Laboratory of Traction Power, Southwest Jiaotong University, Chengdu, People's Republic of China

[2] The State Key Laboratory of Heavy Duty AC Drive Electric Locomotive Systems Integration, Zhuzhou, People's Republic of China

issue in this regard. Therefore, it is extremely important to develop a reliable wear model to predict the evolution of the wheel/rail profiles with the wear.

In the past three decades, numerous papers have reported the investigation of the wheel/rail wear phenomenon, and different wear estimation methodologies have been proposed. Jendel [1] developed a wear prediction tool based on a load collective concept to calculate the wheel wear of the vehicles operating in a commuter rail network in Stockholm. This tool consists of a vehicle model, a railway network definition, and the Archard wear model with the associated wear maps. The vehicle dynamics model is implemented with the GENSYS software. The contact between the wheel and rail is derived based on the Hertz theory and simplified theory of Kalker (FASTSIM algorithm) applied in the normal and tangential directions, respectively. However, the elastic contribution to the creep is neglected. Braghin et al. [2] presented a fast and reliable wear prediction model. In their model, the wear function developed by the University of Sheffield [3, 4] (known as the USFD wear function) was used. Ding et al. [5] proposed a wheel wear model to predict the evolution of the wheel profile shape of heavy-haul freight cars. The semi-Hertzian method [6] and FASTSIM algorithm were used to solve the normal and tangential contact problems, respectively. The wheel wear function proposed by Zobory [7] was used to evaluate the material loss caused by the wear. A powerful wear prediction model was developed and validated by the University of Florence [8–12]. It can be used to evaluate the evolution of both the wheel and rail profiles under wear. The Shen–Hedrick–Elkins theory [13] was used to evaluate the wheel/rail creep force in a dynamic simulation, whereas the simplified theory of Kalker [14] implemented in FASTSIM was employed to solve the local contact problem during wear prediction. Pombo et al. [15] developed a wheel wear computational tool to study the effects of the primary suspension stiffness, rail cant, track/braking forces, and vehicle velocity on the wear progression. This tool implements a dynamic simulation of railway vehicles using VAMPIRE and a post-processing module to predict the wheel wear. Vollebregt et al. [16] demonstrated that the difference of calculated creep forces is obvious by using different rolling contact algorithms, particularly in the case of large-spin creepage, which represents a wheel flange root or wheel flange contact with the rail gauge corner. This situation usually occurs when a train operates on tight curved tracks. Zhang et al. [17] developed an online wheel wear model based on a combination of a multi-body dynamic model and Archard wear theory by performing a SIMPACK and MATLAB/Simulink co-simulation to assess the HXN5 locomotive wheel wear. However, the wheel profile remained unchanged during the simulation. Li et al. [18] proposed a novel model to simulate the wheel wear. In this model, the coupling dynamics of a railway vehicle and track was used to predict the dynamic response. The vehicle was modeled as a multi-body system with 35 degrees of freedom (DOFs). The track was a flexible three-layer model consisting of rails, sleepers, and a ballast bed. The rails were modeled as Euler beams discretely supported by sleepers. The Shen–Hedrick–Elkins model was adopted to solve the tangential contact problem in dynamic simulations. The necessary quantities for the wear prediction were collected after performing a dynamic simulation. Subsequently, they were taken as inputs in post-processing to estimate the wheel wear, where the modified CONTACT code of Kalker [19] was used to recalculate the tangential contact, whereas the Archard wear model was used in the local wear calculation. Jin et al. [20] suggested a rail wear prediction method. The proposed model considered a combination of the non-Hertzian rolling contact theory of Kalker, a rail material wear model, the coupling dynamics of a vehicle and track, and a three-dimensional contact geometry analysis of the wheel–rail pair. The rail wear was also calculated offline. The effect of the rail flexibility on the wheel wear prediction was investigated by Aceituno et al. [21]. The rails were modeled using a finite element floating frame as the reference approach and modal reduction techniques, whereas the subrail foundation was ignored.

In the above literature, either the track flexibility was ignored, or the wear estimation was achieved in the post process rather than in the online solution. With increasing train speed and axle load, the dynamic interaction between the vehicle and track is intensified. Some previous research work indicated that the track flexibility cannot be neglected; this has a significant effect on the wheel/rail contact behavior [22–24], such as wheel/rail contact positions, creepages, spin, and creep forces. These quantities are closely related with the wear estimation. Moreover, a fast, simple contact algorithm in the dynamic simulation and a rigorous model in the wear estimation were employed in numerous wear prediction models. The use of different contact models in the dynamics simulation and wear estimation could not ensure that the contact forces used in the wear calculation satisfied the equilibrium equations in the dynamic simulation.

The objective of this study is to develop a new online wheel wear model by considering the track flexibility. The proposed model consists of two submodels: a locomotive/track coupled dynamics model and a model for the wear estimation. The two submodels interact with each other. The three-dimensional (3D) coupled locomotive/track dynamics model includes three subsystems: a locomotive, ballasted track, and wheel/rail contact. The track flexibility is considered in the current model. The wheel wear estimation model proposed in this paper can be employed in online solutions rather than in post-processing. The wheel wear is estimated at each integrated time step. The wheel profile is updated per revolution, which resembles an actual situation. The effect of the track flexibility on the wear estimation is analyzed, and the results are compared with those obtained using a rigid track. The effect of the wheel profile updating strategy on the wheel wear is also investigated. Some references reported that the traction control strategies and contact conditions have a considerable effect on the wheel/rail wear and curving behavior [25–27]. However, they are out of scope of the current study.

2 Description of a new online wheel wear model

A new online wheel wear model taking into account the track flexibility is proposed. The model consists of two parts that interact with each other, as shown in Fig. 1. In this model (a) a locomotive/track coupled dynamics model and (b) a model for the wear estimation are used. Based on the vertical and lateral vehicle/track coupled dynamics theory [28], a 3D dynamics model of a locomotive coupled with a ballasted track is developed. The coupled locomotive/track dynamics model includes three subsystems: a locomotive, track, and wheel/rail contact. The flexibility of the components, such as the wheelset, bogie frame, and car body, is ignored in the locomotive subsystem. The track flexibility is considered. The rails are modeled as Timoshenko beams, the sleepers and ballast bed are assumed to be a lumped mass. Equivalent springs and dampers are used to simulate the connections between each part of the track. The wheel/rail contact model is the key subsystem that couples the locomotive subsystem with the track subsystem at the wheel/rail interfaces. The nonlinear Hertzian elastic contact theory is used to estimate the wheel–rail normal contact forces. The simplified theory of Kalker implemented in FASTSIM [14] is used to calculate the tangential wheel–rail creep forces and shear stress distribution. The local creep, shear stress distribution, contact patch dimension, and contact positions are output at each integration step of the locomotive/track coupled dynamics simulation. Subsequently, these quantities are input into the wear estimation model. The wear function considering the energy dissipated in the wheel–rail contact patch with the worn material, developed by University of Sheffield [3, 4], is used to evaluate the amount of material loss and material distribution along the
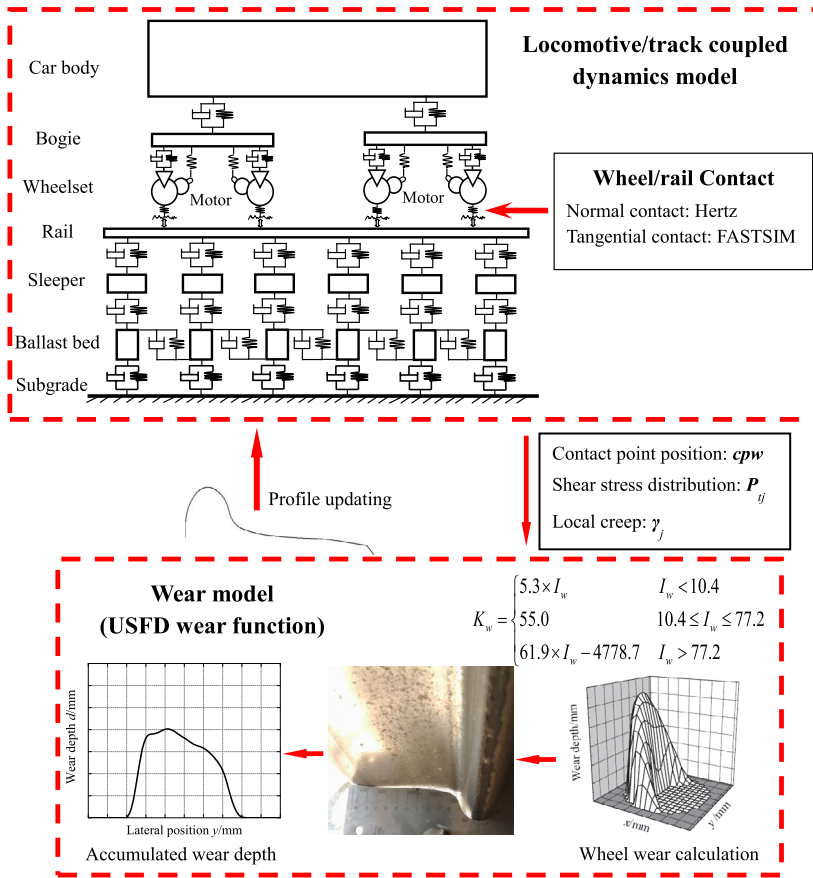
**Fig. 1** Scheme of the wheel wear prediction model

wheel profile. The wheel wear estimation model can be employed in online solutions rather than in post-processing. The wheel wear is estimated at each integrated time step. The wheel profiles are updated per revolution, which mimics an actual situation. The numerical noise and short wavelength contributions are treated with a moving average filter. Then, a spline smoothing is used to smooth the wear distribution and worn wheel profile before the next step.

2.1 Locomotive/track coupled dynamics model

The coupled locomotive/track dynamics model includes three subsystems: a locomotive subsystem, track subsystem, and wheel/rail contact subsystem. Each subsystem is described in this section.

2.1.1 Locomotive subsystem

A high-power locomotive, widely used in China, is selected to be modeled in this study. The locomotive has two bogies with two axles in a Bo–Bo configuration. The model consists of
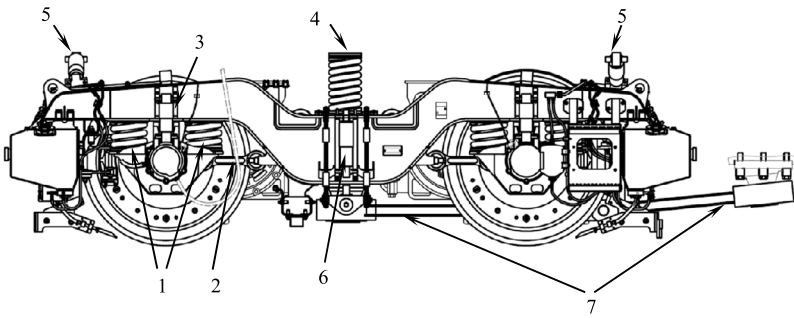
1. primary suspension flexi-coil spring; 2. axle box longitudinal rod; 3. primary suspension vertical damper; 4. secondary suspension flexi-coil spring; 5. secondary suspension lateral damper; 6. secondary suspension vertical damper; 7. traction rod; 8. lateral bump stop (not seen)

**Fig. 2** Side elevation of the bogie

two identical units, Loco A and Loco B. Therefore, only one unit is considered here. Figure 2 shows the elevation of a bogie and suspension elements. This bogie has two stages of suspensions. The primary suspensions are composed of two flexi-coil springs (each axle box) to provide the vertical stiffness, a single longitudinal rod to provide the main longitudinal stiffness and transmit the traction and braking force from the wheelset to the bogie frame, and a nonlinear vertical damper. The secondary suspensions comprise six flexi-coil springs (three for each side) to provide the longitudinal, lateral and vertical stiffness. Two lateral nonlinear dampers are arranged at the end carriage of the bogie (see Fig. 2) to reduce the lateral vibration of the car body. Meanwhile, they also can provide rotary torque to limit the yaw motion of the bogie, which have similar function as the yaw damper. Two vertical nonlinear dampers are arranged at each side of the bogie to reduce the vertical vibration from the bogie to the car body. Additionally, the secondary suspensions also include a traction rod to transmit the longitudinal force, and a nonlinear lateral bump stop to limit the lateral displacement of the bogie. Each wheelset is equipped with an axle-hung motor. The wheelset, bogie frame, and car body have six DOFs, i.e., the longitudinal, lateral, and vertical displacements, and the roll, pitch, and yaw angle. However, only the vertical displacement and pitch motion are considered for the motor. Therefore, the locomotive subsystem is modeled as a 50 DOFs nonlinear multi-body system that includes 11 rigid components: a car body, two bogie frames, four wheelsets, and four motors.

According to the D'Alembert's principle, the motion equations of a locomotive subsystem can be easily derived. These can be expressed in the form of second-order differential equations in the time domain as

$$\mathbf{M}\ddot{\mathbf{X}} + \mathbf{C}\dot{\mathbf{X}} + \mathbf{K}\mathbf{X} = \mathbf{F}_{\text{IN}} + \mathbf{F}_{\text{EXT}}, \tag{1}$$

where $\mathbf{X}$, $\dot{\mathbf{X}}$ and $\ddot{\mathbf{X}}$ are the vectors of the displacements, velocities, and accelerations of the locomotive subsystem, respectively; $\mathbf{M}$ is the mass matrix of the locomotive; $\mathbf{C}$ and $\mathbf{K}$ are the damping and stiffness matrices of the suspension elements, respectively; $\mathbf{F}_{\text{IN}}$ is the system load vector representing the nonlinear wheel/rail contact forces; and $\mathbf{F}_{\text{EXT}}$ represents the external forces, including the gravity and forces resulting from the centripetal acceleration during curve negotiation, as well as the traction and braking forces. The suspension elements include linear and nonlinear elements. The damping and stiffness are not constant for the nonlinear elements. The damping of the nonlinear dampers depends on the relative velocity

Fig. 3 The nonlinear
characteristics of the dampers
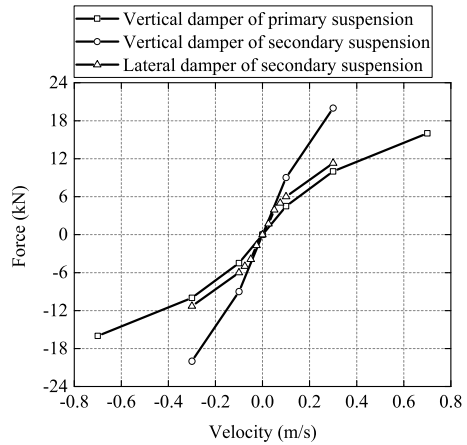
Fig. 4 Serial spring–damper
force element used to represent a
damper
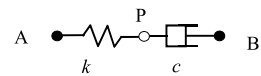
of the two ends of the element, and the stiffness of the lateral bump stop depends on the relative displacement of its two ends. The damping and stiffness matrices **C** and **K** in (1) vary with time for the terms of nonlinear suspension elements.

All the dampers, such as the vertical damper of the primary and secondary suspensions and lateral dampers of the secondary suspensions, are modeled as serial spring–damper force elements, and their nonlinear characteristics are considered (see Fig. 3). The distance between two connect points (point A and B in Fig. 4) of the force element is assumed as l. The initial length of the spring is l_0, and its length is l_1 after deformation. The damper length is l_2. The inertia of the damper is ignored. Spring force F_s and damper force F_d at point P are equivalent. Therefore, the force element has the following relation:

$$l = l_1 + l_2, \tag{2}$$

$$F_s = F_d, \quad F_s = k(l_1 - l_0), \quad F_d = c\dot{l}_2, \tag{3}$$

where k is the rubber joint stiffness and c is the damping of the damper. The damping is nonlinear, and its value depends on the velocity of the two connect points.

The first derivative of (2) can be written as

$$\dot{l} = \dot{l}_1 + \dot{l}_2. \tag{4}$$

From (2)–(4), we can obtain the following first-order differential equation

$$c\dot{l}_2 + kl_2 = k(l - l_0). \tag{5}$$

Equation (5) can be solved with the motion of equations of the locomotive subsystem.

The lateral bump stop installed on the secondary suspension is modeled using a bilinear spring element. The force of the lateral bump stop is

$$F_{yST} = \begin{cases} 0, & |\Delta y_{ST}| < \delta, \\ K_{ST}(|\Delta y_{ST}| - \delta), & |\Delta y_{ST}| \geq \delta, \end{cases} \tag{6}$$

Table 1 Main parameters of the electric locomotive used in the simulation

Notation	Parameter	Value
M_c	Car body mass (kg)	61882
M_t	Bogie mass (kg)	4698.5
M_w	Wheelset mass (kg)	3562
M_m	Motor mass (kg)	1100.5
I_{cx}	Mass moment of inertia of car body about X axis (kg m^2)	95970
I_{cy}	Mass moment of inertia of car body about Y axis (kg m^2)	1539900
I_{cz}	Mass moment of inertia of car body about Z axis (kg m^2)	1536740
I_{tx}	Mass moment of inertia of bogie frame about X axis (kg m^2)	2260
I_{ty}	Mass moment of inertia of bogie frame about Y axis (kg m^2)	8480
I_{tz}	Mass moment of inertia of bogie frame about Z axis (kg m^2)	10360
I_{wx}	Mass moment of inertia of wheelset about X axis (kg m^2)	2064
I_{wy}	Mass moment of inertia of wheelset about Y axis (kg m^2)	573
I_{wz}	Mass moment of inertia of wheelset about Z axis (kg m^2)	2064
I_{mx}	Mass moment of inertia of motor about X axis (kg m^2)	320
I_{my}	Mass moment of inertia of motor about Y axis (kg m^2)	350
I_{mz}	Mass moment of inertia of motor about Z axis (kg m^2)	320
K_{px}	Primary suspension stiffness along X axis (MN/m)	40.83
K_{py}	Primary suspension stiffness along Y axis (MN/m)	4.83
K_{pz}	Primary suspension stiffness along Z axis (MN/m)	2.91
K_{sx}	Secondary suspension stiffness along X axis (MN/m)	0.6975
K_{sy}	Secondary suspension stiffness along Y axis (MN/m)	0.6975
K_{sz}	Secondary suspension stiffness along Z axis (MN/m)	1.671
K_{mz}	Stiffness of motor suspend along Z axis (MN/m)	95
K_{tx}	Traction rod stiffness along X axis (MN/m)	50
K_{ty}	Traction rod stiffness along Y axis (MN/m)	50

where K_{ST} is the contact stiffness when the car body contacts the bump stop, Δy_{ST} is the lateral relative displacement between the car body and bogie frame at the position of the bump stop, and δ is the lateral clearance between the car body and bump stop in the bogie frame.

The flexi-coil spring with primary and secondary suspensions, the longitudinal rod of primary suspension, the traction rod for secondary suspensions and the motor suspender are modeled as 3D linear spring force elements. The main parameters of the electric locomotive used in the simulation are listed in Table 1.

2.1.2 Track subsystem

The track flexibility is considered in the current model. The rails are modeled as Timoshenko beams, discretely supported by sleepers. Each sleeper is assumed to be a lumped mass, and the lateral, vertical, and roll motions are considered. The ballast bed is treated as equivalent rigid ballast bodies. Only the vertical motion of the ballast bed is considered. Equivalent springs and dampers are employed as the connections between each part of the track.

Using the modal superposition method and normalized shape function of a Timoshenko beam, the fourth-order partial differential equations of the rails are converted into second-order ordinary differential equations as follows [29, 30]:

(Lateral vibration)

$$
\begin{cases}
\ddot{q}_{yk}(t) + \dfrac{\kappa_{ry} G_r A_r}{m_r}\left(\dfrac{k\pi}{l_r}\right)^2 q_{yk}(t) - \kappa_{ry} G_r A_r \dfrac{k\pi}{l_r}\sqrt{\dfrac{1}{m_r \rho_r I_{rz}}}\, w_{yk}(t) \\[2mm]
\quad = \sqrt{\dfrac{2}{m_r l_r}}\left[\displaystyle\sum_{i=1}^{N_W}\sin\left(\dfrac{k\pi}{l_r}x_{wi}\right)F_{wryi}(t) - \sum_{j=1}^{N_S}\sin\left(\dfrac{k\pi}{l_r}x_{sj}\right)F_{rsyj}(t)\right], \\[4mm]
\ddot{w}_{yk}(t) + \left[\dfrac{\kappa_y G_r A_r}{\rho_r I_{rz}} + \dfrac{E_r I_{rz}}{\rho_r I_{rz}}\left(\dfrac{k\pi}{l_r}\right)^2\right]w_{yk}(t) - \kappa_{ry} G_r A_r \dfrac{k\pi}{l_r}\sqrt{\dfrac{1}{m_r \rho_r I_{rz}}}\, q_{yk}(t) = 0 \\[3mm]
(k = 1, \ldots, N_L),
\end{cases}
\tag{7}
$$

(Vertical vibration)

$$
\begin{cases}
\ddot{q}_{zk}(t) + \dfrac{\kappa_{rz} G_r A_r}{m_r}\left(\dfrac{k\pi}{l_r}\right)^2 q_{zk}(t) - \kappa_{rz} G_r A_r \dfrac{k\pi}{l_r}\sqrt{\dfrac{1}{m_r \rho_r I_{ry}}}\, w_{zk}(t) \\[2mm]
\quad = \sqrt{\dfrac{2}{m_r l_r}}\left[\displaystyle\sum_{i=1}^{N_W}\sin\left(\dfrac{k\pi}{l_r}x_{wi}\right)F_{wrzi}(t) - \sum_{j=1}^{N_S}\sin\left(\dfrac{k\pi}{l_r}x_{sj}\right)F_{rszj}(t)\right], \\[4mm]
\ddot{w}_{zk}(t) + \left[\dfrac{\kappa_{rz} G_r A_r}{\rho_r I_{ry}} + \dfrac{E_r I_{ry}}{\rho_r I_{ry}}\left(\dfrac{k\pi}{l_r}\right)^2\right]w_{zk}(t) - \kappa_{rz} G_r A_r \dfrac{k\pi}{l_r}\sqrt{\dfrac{1}{m_r \rho_r I_{ry}}}\, q_{zk}(t) = 0 \\[3mm]
(k = 1, \ldots, N_V),
\end{cases}
\tag{8}
$$

(Torsional vibration)

$$
\ddot{q}_{Tk}(t) + \dfrac{G_r K_r}{\rho_r I_{r0}}\left(\dfrac{k\pi}{l_r}\right)^2 q_{Tk}(t) = \sqrt{\dfrac{2}{\rho_r I_{r0} l_r}}\left[\sum_{i=1}^{N_W}\sin\left(\dfrac{k\pi}{l_r}x_{wi}\right)M_{wri}(t)\right.
$$
$$
\left. - \sum_{j=1}^{N_S}\sin\left(\dfrac{k\pi}{l_r}x_{sj}\right)M_{rsj}(t)\right] \quad (k = 1, \ldots, N_T).
\tag{9}
$$

In (7)–(9), $q_{yk}(t)$, $q_{zk}(t)$, and $q_{Tk}(t)$ are the generalized coordinates of the lateral, vertical, and rotational deformation of the rail, respectively, and $w_{yk}(t)$ and $w_{zk}(t)$ are the generalized coordinates of the deflection curve of the rail with respect to the z-axis and y-axis, respectively. The material properties of the rail are determined by density ρ_r, shear modulus G_r, and Young's modulus E_r; m_r is the mass per unit longitudinal length. The geometry of the cross-section of the rail is represented by area A_r, second moments of area I_{ry} and I_{rz} around the y-axis and z-axis, respectively, and polar moment of inertia I_{r0}; κ_{ry} and κ_{rz} are the shear coefficients for the lateral and vertical bending, respectively, and $G_r K_r$ is the rail torsional stiffness. The calculation length of the rail is denoted by l_r; F_{rsyj} and F_{rszj} are the lateral and vertical forces between the rail and sleeper j, respectively. The wheel/rail forces at wheel i in the lateral and vertical directions are represented by F_{wryi} and F_{wrzi}, respectively; M_{rsj} and M_{wri} denote the equivalent moments acting on the rail; x_{sj} and x_{wi} denote

Table 2 Main parameters of the ballasted track used in the simulation

Notation	Parameter	Value (per rail seat)
E_r	Elastic modulus of rail (N/m^2)	2.059×10^{11}
ρ_r	Density of rail (kg/m^3)	7.86×10^3
I_{r0}	Torsional inertia of rail (m^4)	3.741×10^{-5}
I_y	Rail second moment of area about Y axis (m^4)	3.217×10^{-5}
I_z	Rail second moment of area about Z axis (m^4)	5.24×10^{-6}
m_r	Rail mass per unit length (kg/m)	60.64
$G_r K_r$	Rail torsional stiffness (N m/rad)	1.9587×10^5
κ_{ry}	Rail lateral bending shear coefficient	0.4057
κ_{rz}	Rail vertical bending shear coefficient	0.5329
M_s	Sleeper mass (half) (kg)	125.5
K_{pv}	Fastener stiffness in vertical direction (N/m)	6.5×10^7
K_{ph}	Fastener stiffness in lateral direction (N/m)	2.0×10^7
C_{pv}	Fastener damping in vertical direction (N s/m)	7.5×10^4
C_{ph}	Fastener damping in lateral direction (N s/m)	5.0×10^4
l_s	Sleeper spacing (m)	0.545
l_e	Effective support length of half sleeper (m)	0.95
l_b	Sleeper width (m)	0.273
ρ_b	Ballast density (kg/m^3)	1.8×10^3
E_b	Elastic modulus of ballast (Pa)	1.1×10^8
C_b	Ballast damping (N s/m)	5.88×10^4
K_w	Ballast shear stiffness (N/m)	7.84×10^7
C_w	Ballast shear damping (N s/m)	8.0×10^4
α	Ballast stress distribution angle (°)	35
h_b	Ballast thickness (m)	0.45
E_f	Subgrade $K30$ modulus (Pa/m)	9.0×10^7
C_f	Subgrade damping (N s/m)	3.115×10^4

the longitudinal positions of sleeper j and wheel I; N_w and N_s are the number of wheelsets and sleepers within the analyzed rail, respectively. Subscript j represents a sleeper j and i for wheel i; N_L, N_V, and N_T are the total numbers of shape functions.

It is easy to establish the equations of motion of the sleepers and ballast masses by applying the D'Alembert's principle. For brevity, the differential equations of the sleeper and ballast bodies are omitted in this paper. The main parameters of the track used in the simulation are listed in Table 2 [23, 29].

The "Tracking Window" model developed by Xiao et al. [31] is used to take into account the effects of discrete support. The locomotive/track system is a large-scale dynamic system. The motions of the system are described by nonlinear equations. They have to be solved by numerical solution. In order to balance the calculation efficiency and accuracy, a simple fast explicit integration method proposed by Zhai is employed [32].

2.1.3 Wheel/rail contact subsystem

The wheel/rail contact is a key part of the locomotive/track coupling dynamics model that couples the locomotive subsystem with the ballasted track subsystem. The main purpose

of the wheel/rail contact model is to determine the wheel/rail contact position and contact forces between the wheel and rail interface. The contact point on the wheel and rail surface is calculated based on an improved geometric calculation model of the wheel/rail contact discussed in [19].

The wheel/rail normal contact forces are estimated by the Hertzian nonlinear elastic contact theory, which is written as [33]

$$P(t) = \begin{cases} [\frac{1}{G}\delta_i(t)]^{3/2}, & \delta_i(t) > 0, \\ 0, & \delta_i(t) \le 0, \end{cases} \tag{10}$$

where $\delta_i(t)$ is the normal elastic compression deformation of the wheels and rails at the contact points; G is the wheel/rail contact constant, and it is different for conical profiles and worn-shaped profiles, which is written as [33]

$$G = \begin{cases} 4.57R^{-0.149} \times 10^{-8} \ (\text{m/N}^{2/3}), & \text{for conical profile,} \\ 3.86R^{-0.115} \times 10^{-8} \ (\text{m/N}^{2/3}), & \text{for worn-shaped profile,} \end{cases} \tag{11}$$

where R is the wheel radius (m).

With the purpose of developing a local online wheel wear prediction model, the simplified theory of Kalker [14] implemented in FASTSIM is employed to calculate the tangential wheel/rail contact forces, tangential stresses, and local creep distribution within the contact patch. In the FASTSIM algorithm, the tangential stress distribution is evaluated by the numerical integration over the contact patch area from the leading edge to the trailing edge. In the longitudinal integration region the tangential stresses are calculated as follows:

$$\begin{cases} p_x(x - \Delta x, y_i) = p_x(x, y_i) - \Delta p_x, \\ p_y(x - \Delta x, y_i) = p_y(x, y_i) - \Delta p_y, \end{cases} \tag{12}$$

where p_x and p_y are the longitudinal and lateral stresses, respectively; $(x - \Delta x, y_i)$ and (x, y_i) are the particles in the current and previous integration step, respectively; Δx is the mesh length in the longitudinal directions so that p_x and p_y are equal to zero for a particle at the leading edge; and Δp_x and Δp_y are the stress increments in the longitudinal and lateral directions, respectively, and they are written as

$$\begin{cases} \Delta p_x = \left(\dfrac{\xi_x}{L_x} - \dfrac{\xi_\eta y_i}{L_\varphi} \right)\Delta x, \\ \Delta p_y = \left[\dfrac{\xi_y}{L_y} + \dfrac{\xi_\eta(2x - \Delta x)}{2L_\varphi} \right]\Delta x, \end{cases} \tag{13}$$

where ξ_i for $i = x, y, \eta$ are the longitudinal, lateral, and spin creepages, respectively; L_i, $i = x, y, \eta$, are the longitudinal, lateral and spin flexibility parameters, respectively.
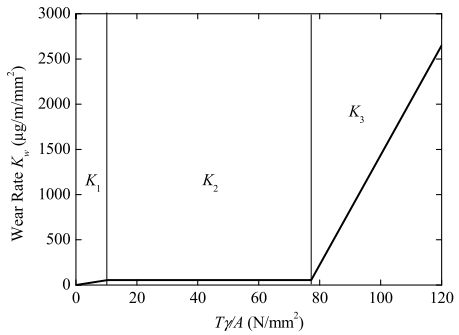
The local stress magnitude at the current integration particle is

$$p_t(x - \Delta x, y_i) = \sqrt{\left[p_x(x - \Delta x, y_i) \right]^2 + \left[p_y(x - \Delta x, y_i) \right]^2}. \tag{14}$$

The traction bound in FASTSIM is determined by the parabolic normal traction and friction coefficient

$$p_3(x - \Delta x, y_i) = \frac{2P}{\pi ab} \left(1 - \frac{x_i^2}{a^2} - \frac{y_i^2}{b^2} \right). \tag{15}$$

Fig. 5 Wear rate as a function of the wear index

If the local stress magnitude does not exceed the traction bound, which implies the particle is in the stick zone, the tangential stresses can be calculated with (12), and the corresponding local creep is equal to zero. On the contrary, if the actual particle is in the slip zone, the stress is reduced according to

$$
\begin{cases}
p_{xs}(x - \Delta x, y_i) = \left[p_x(x, y_i) - \Delta p_x \right] \dfrac{\mu p_3(x - \Delta x, y_i)}{p_t(x - \Delta x, y_i)}, \\[4mm]
p_{ys}(x - \Delta x, y_i) = \left[p_y(x, y_i) - \Delta p_y \right] \dfrac{\mu p_3(x - \Delta x, y_i)}{p_t(x - \Delta x, y_i)}.
\end{cases}
\tag{16}
$$

The local creep including the elastic contribution can be calculated according to [34]

$$
\begin{cases}
\omega_x = \dfrac{L_x}{\Delta x} \left[p_{xs}(x - \Delta x, y_i) - p_x(x - \Delta x, y_i) \right], \\[4mm]
\omega_y = \dfrac{L_y}{\Delta x} \left[p_{ys}(x - \Delta x, y_i) - p_y(x - \Delta x, y_i) \right].
\end{cases}
\tag{17}
$$

2.2 Wear model

The wear function considering the energy dissipated in the wheel/rail contact patch with a worn material, developed by the University of Sheffield [3, 4], is used to evaluate the wheel wear. Three wear regimes are defined in the wear function, i.e., mild wear, severe wear, and catastrophic wear corresponding to K_1, K_2, and K_3 regimes in Fig. 5. The analytical expression for wear rate K_w (µg/m/mm^2), which expresses the weight loss in the material (µg) per distance rolled (m) per contact area (mm^2), is given by the following equation [3, 4]:

$$
K_w = \begin{cases}
5.3 \times I_w, & I_w < 10.4, \\
55.0, & 10.4 \leq I_w \leq 77.2, \\
61.9 \times I_w - 4778.7, & I_w > 77.2,
\end{cases}
\tag{18}
$$

where I_w (N/mm^2) is the local frictional power in the contact patch and can be written as

$$
I_w(x, y) = p(x, y) \cdot \gamma(x, y)
\tag{19}
$$

where $p(x, y)$ and $\gamma(x, y)$ are the traction stresses and local creep in each point (x, y) of the contact patch particle, respectively.

After estimating the wear rate, wear distribution $\delta_{p(t)}(x, y)$ in each point (x, y) of the contact patch particle can be calculated as

$$\delta_{p(t)}(x, y) = \frac{K(I_w)}{\rho} \Delta x, \tag{20}$$

where ρ is the material density of the wheel material (expressed in kg/m^3) and Δx is the length of the meshes of the contact patch in the longitudinal direction.

Then, all the wear contributions within contact patch are summed in the longitudinal direction. The wear distribution at one cross-section is achieved as

$$\delta_{p(t)}^{\text{tot}}(y) = \int_{-a(y)}^{+a(y)} \delta_{p(t)}(x, y)\, dx. \tag{21}$$

Lastly, the wear distribution during the dynamic simulation is summed to get

$$W_d(y) = \frac{1}{2\pi R} \int_{T_{\text{start}}}^{T_{\text{end}}} \delta_{p(t)}^{\text{tot}}(y) v\, dt, \tag{22}$$

where R is the nominal rolling radius, v is the vehicle speed, and T_{start} and T_{end} are the starting and the ending time of the simulation.

3 Simulation results

3.1 Validation of the locomotive/track dynamics model

The locomotive/track coupled dynamics model was validated by field measurement results. The straight line running test was conducted at a loop railway line at the China Academy of Railway Sciences. The track structure in the experimental section is a typical ballast track widely used in China, conventionally the speed railway line. The rails are Chinese, 60 kg/m. Type II concrete sleepers are used, and the rail cant is 1/40. The test speeds of 80, 100, 110, 120, and 132 km/h are tested. The main results such as the derailment coefficient, rate of wheel load reduction, car body acceleration, and Sperling index from the dynamics performance test are given here, and compared with those obtained from the locomotive/track dynamics model. Owing to the lack in actual track irregularities at the test section, the track random irregularity of China Railway mainlines [23] is used in the current study. Speed ranges from 80 to 135 km/h with an interval of 5 km/h in the simulation are studied. The track flexibility is considered during the model validation.

Figure 6(a) and (b) show the maximum values of the derailment coefficient and rate of wheel load reduction, respectively. The derailment coefficient, namely Nadal coefficient, defined as the ratio of the lateral force to the total vertical force on the same wheel (Q/P) [35]. The rate of wheel load reduction (wheel unloading ratio) [33] is defined as the ratio of the reduction in the vertical dynamical forces on both wheels of a wheelset to the total vertical wheelset loading. It can be calculated as

$$R_{\text{wheel\_unloading}} = \frac{\bar{P} - P}{\bar{P}}, \tag{23}$$

where P is the vertical force and $\bar{P}$ is the static vertical force. If $P < \bar{P}$, the wheel unloading ratio will be calculated.
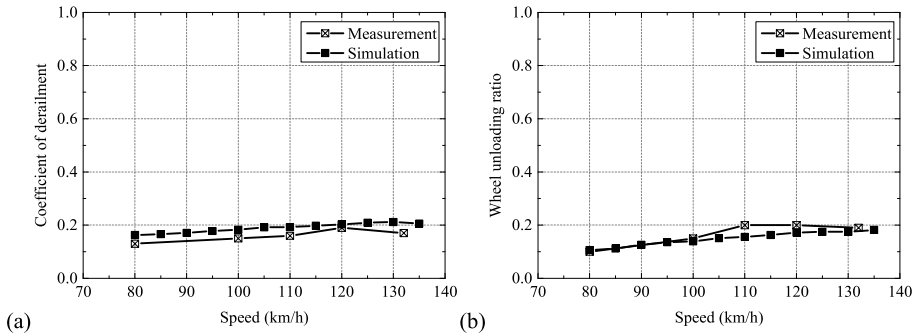
Fig. 6 Comparison of the measured and simulated (**a**) coefficient of derailment and (**b**) rate of wheel load reduction on a straight track
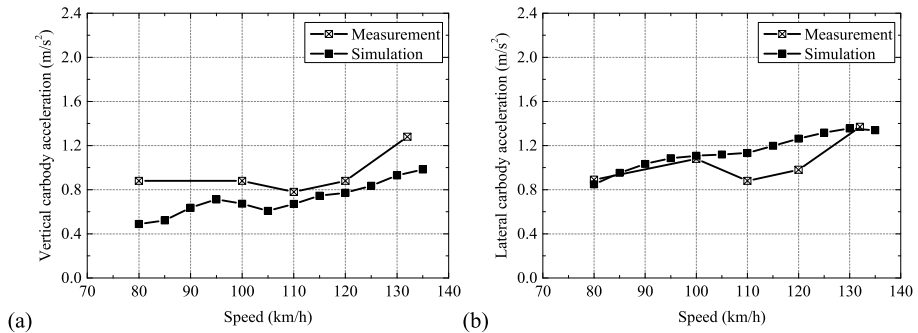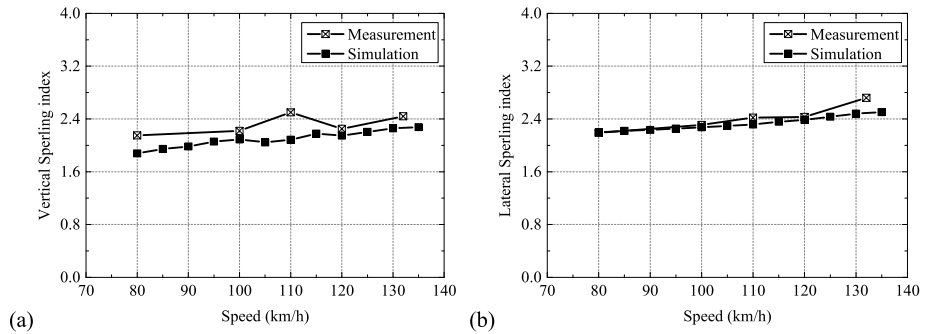

Fig. 7 Comparison of the measured and simulated (**a**) vertical and (**b**) lateral car body acceleration on a straight track

The instrumented wheelset was used to measure the lateral and vertical wheel/rail forces during the test. After obtaining the wheel/rail forces, the derailment coefficient and wheel unloading ratio can be calculated through the wheel/rail forces. Both the measurement and simulation results indicate that the derailment coefficient and rate of wheel load reduction increase with speed. The derailment coefficients obtained from the simulations are slightly larger than those of the measurement. Both the rates of wheel load reduction are in good agreement.

The maximum car body acceleration and Sperling ride comfort index are chosen for the comparison of the locomotive dynamic responses. The Sperling index could be calculated with Sperling's method based on the car body accelerations and weighted by frequencies [36]. The comparison results are illustrated in Figs. 7 and 8. The results indicate that the vertical car body acceleration and vertical Sperling index of the simulation are slightly smaller than those of the measurement, whereas the lateral car body acceleration and lateral Sperling index are in reasonable agreement for the simulation and measurement.

Time histories of the derailment coefficient during the locomotive curving negotiation are also compared, as shown in Fig. 9. The instrumented wheelset was used to measure the lateral and vertical wheel/rail forces. Then the coefficient of derailment can be obtained through the wheel/rail forces. A low pass filter with 40 Hz was used to filter the results. The curve radius is 300 m with a super-elevation of 140 mm. The locomotive speed is

Fig. 8 Comparison of the measured and simulated (**a**) vertical and (**b**) lateral Sperling index on a straight track
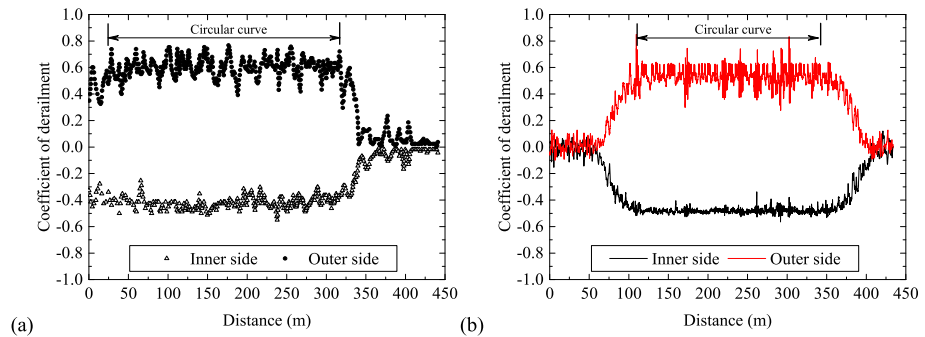
Fig. 9 Comparison of the (**a**) measured and (**b**) simulated coefficient of derailment on a curved track with a radius of 300 m. The locomotive speed is 70 km/h

70 km/h. The locomotive speed, the radius of circular curved track and super-elevation in the simulation coincided with the actual situation, while the length of each part of the curved track of the test section was unknown. The simulated coefficient of derailment is in good agreement with the measured one for both the inner and outer side wheel in the circular curved track. The start position of the measured results may be at the circular curved track, however, a complete curved track, including 50 m straight track, 60 m transition curve, 230 m circular curved track, 60 m transition curve and 30 m straight track, is considered in the simulation. It can be seen from these figures that the time responses of the derailment coefficient estimated by the locomotive/track coupled dynamics model agree well with the field measurement results.

The wheel–rail profiles are the standard profiles in the simulation, which may have same difference with the actual ones after wear. Moreover, the track irregularities and the friction coefficient are hypothetical, and the traction/braking action are ignored. It is inevitable to have some difference between the simulation and measurement results. The tendency of the simulation results are coincided with the measured ones. Comparing the simulation results with the field measurement results proves that the numerical simulation model developed herein is reasonable.

Table 3 Curved tracks with small radii for Case 1

Radius (m)	Super-elevation (mm)	Speed (km/h)	Total length (m)
300	142	60	1090
400	106	60	1090
600	71	60	1090
800	53	60	1090

Table 4 Curved tracks with large radii for Case 2

Radius (m)	Super-elevation (mm)	Speed (km/h)	Total length (m)
1000	76	80	1090
2000	38	80	1090
3000	25	80	1090
4000	19	80	1090

3.2 Effects of track flexibility on wheel wear

To investigate the effect of track flexibility and wheel profile updating strategy on the wheel wear, two simulation cases are studied. For Cases 1 and 2, a series of idealized curved tracks with small and large radii are designed and given in Tables 3 and 4, respectively. The tracks considered in the present study consist of 50 m straight tracks, 80 m transition curve, 800 m circular curved track, 80 m transition curve, and 80 m straight track. The total length of the track is 1090 m. The operating speed of the locomotive is assumed to be constant during the simulation. The traction and braking forces are ignored. The track random irregularity of China Railway mainlines [23] is used in the current study.

In the classical vehicle dynamics model, the track flexibility is ignored. However, some field measurement and numerical results indicate that the track flexibility has a significant effect on the vehicle and track dynamic response [23], particularly for wheel/rail contact forces, which are necessary for wheel wear prediction. The axle load of the electric locomotive, modeled in this paper, is 25 tons. With increasing axle load, the dynamic interaction between the locomotive and track cannot be neglected. In this section, the difference in the wheel/rail interaction and wheel wear between the flexible track and rigid track will be investigated in detail.

3.2.1 Wheel/rail interaction

Not only the locomotive dynamic response, but also the track dynamic response can be considered in the locomotive/track coupling dynamics model developed herein. Figure 10 illustrates the time history of the lateral rail displacement and rail roll displacement under the first wheelset during a curve negotiation simulated by the flexible track model. The curve radius is 300 m, but the circular part is only 200 m, and the other parameters are the same as those listed in Table 3. It can be seen from Fig. 10 that the high rail and low rail are squeezed outward by the lateral wheel–rail forces in the process of curve negotiation, and the maximum lateral displacement of the rail reaches 2.04 mm. The maximum dynamic rail gauge widening is 2.37 mm in this case. Moreover, the rail roll displacement is also obvious, and the maximum absolute value is about 5 mrad for the high rail. The rail roll motion is equivalent to the change of rail cant. The rail cant in the simulation is 1/40, that means the inclined angle of the high rail is about 25 mrad. At this situation, the rail roll motion
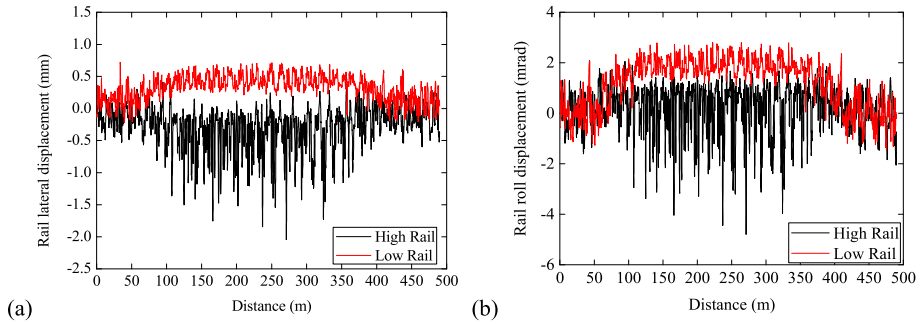
Fig. 10 Time history of the (**a**) rail lateral displacement and (**b**) rail roll displacement during curve negotiation
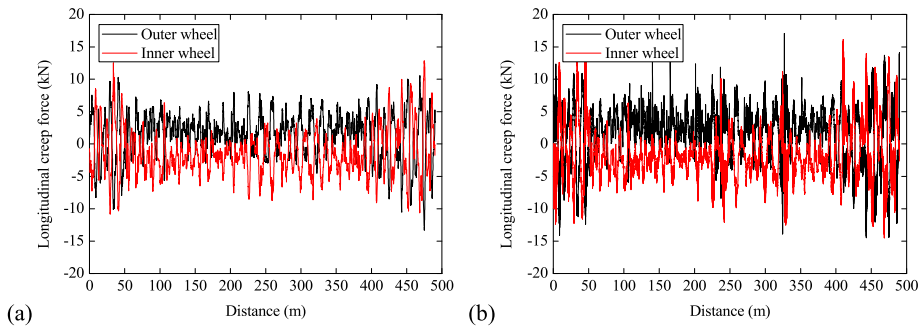
Fig. 11 Comparison of the longitudinal creep force of the leading wheelset of the first bogie between the (**a**) flexible and (**b**) rigid track

is equivalent to the rail cant changes from 1/40 to 1/50 for the high rail. The variation in the rail gauge and rail roll displacement will inevitably lead to a change in the wheel rail contact geometry relationship, creepages, and creep forces. This effect is taken into account in current locomotive/ track coupled model.

Figures 11 and 12 compare the longitudinal and lateral creep forces of the first wheelset of a locomotive curving on flexible and rigid track models, respectively. The results indicate that both longitudinal and lateral creep forces predicted with a flexible track model are generally smaller than those with a rigid track model, which is in agreement with the conclusions published in [23]. Figure 13 shows the wear numbers ($T\gamma$) calculated with the flexible track model and rigid track model. It can be seen from the results that there is a significant difference between the two models. The wear number variation of the rigid model is larger than that of the flexible model. Therefore, the wheel wear predicted by the two models may have an obvious difference.

3.2.2 Wheel wear

Figures 14 and 15 compare the wear spreading of the leading wheelset on the curved tracks with small and large radii, defined in Tables 3 and 4, respectively. The wear spreading shapes predicted with the flexible and rigid track models are very similar, but the maximum wear depth has some difference, particularly for the outer wheel of the curved tracks with a small
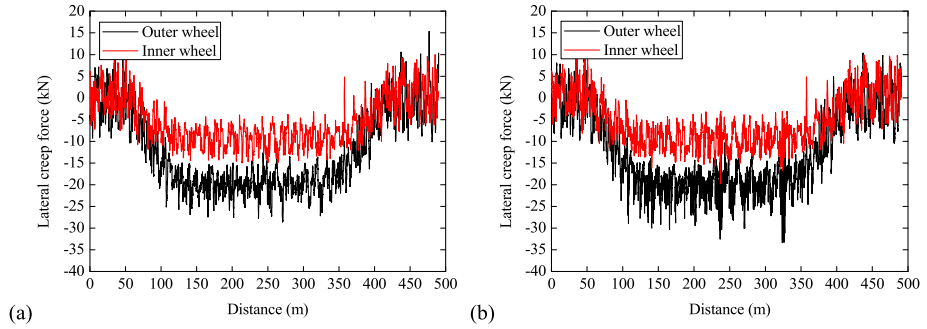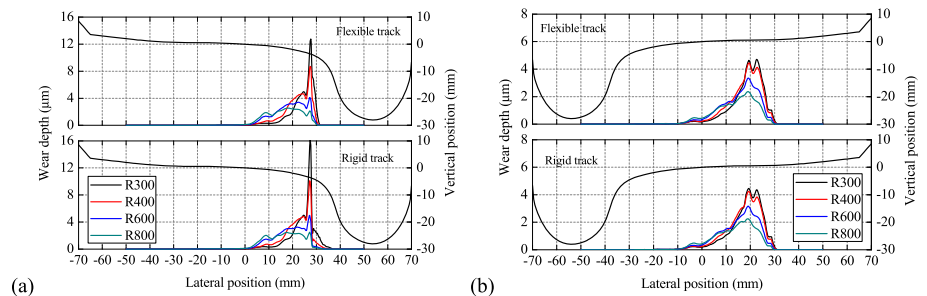
Fig. 12 Comparison of the lateral creep force of the leading wheelset of the first bogie between the (**a**) flexible and (**b**) rigid track model
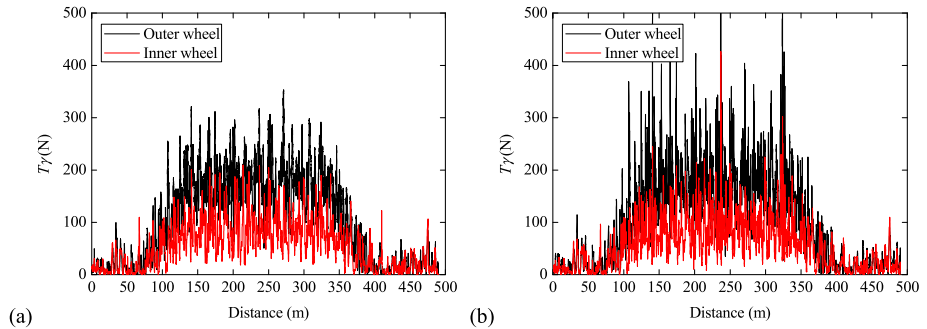

Fig. 13 Comparison of the wear index of the leading wheelset of the first bogie between the (**a**) flexible and (**b**) rigid track model
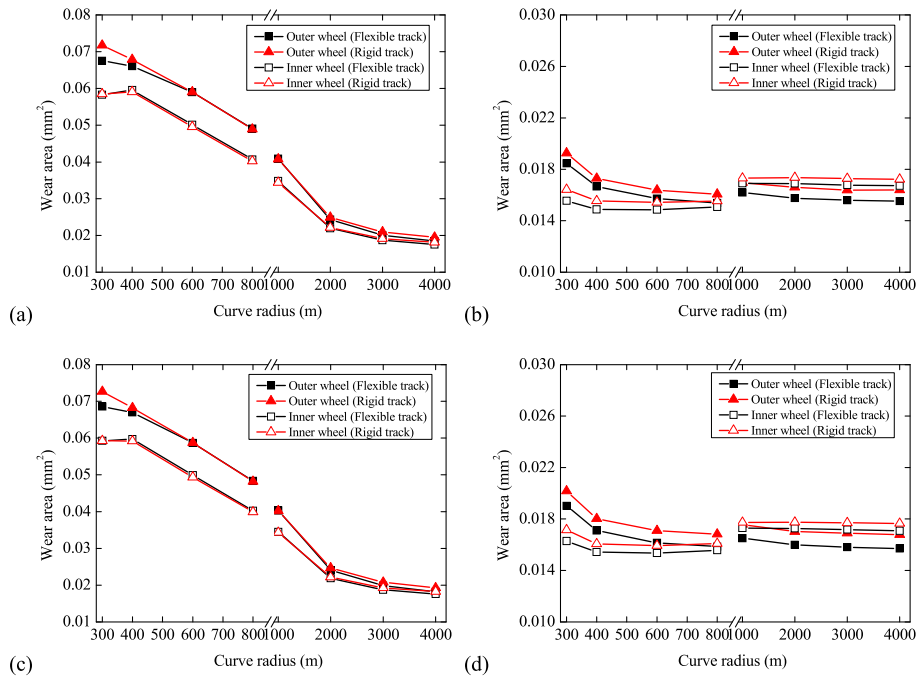

Fig. 14 Comparison between the flexible and rigid track models based on the leading wheelset wear depths on curved tracks with small radii: (**a**) outer wheel and (**b**) inner wheel

radii. The maximum wear depth for a flexible track model is 12.8 μm for R300, whereas the value is 16.2 μm for the rigid track model for the same case. The reason is that the creep forces and creepages obtained by the rigid track model are larger than those by the flexible track model, which results in the obvious difference in the frictional power. Finally, the wear
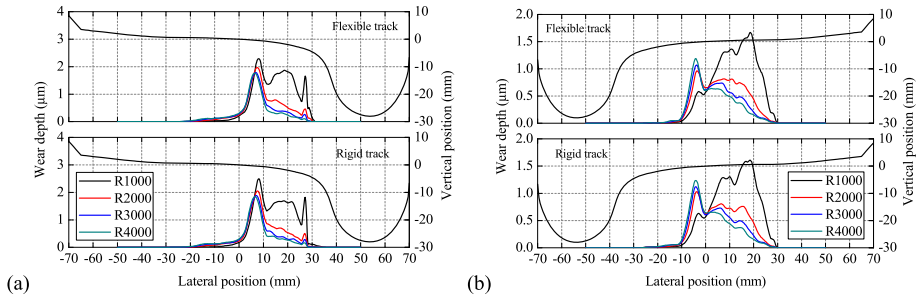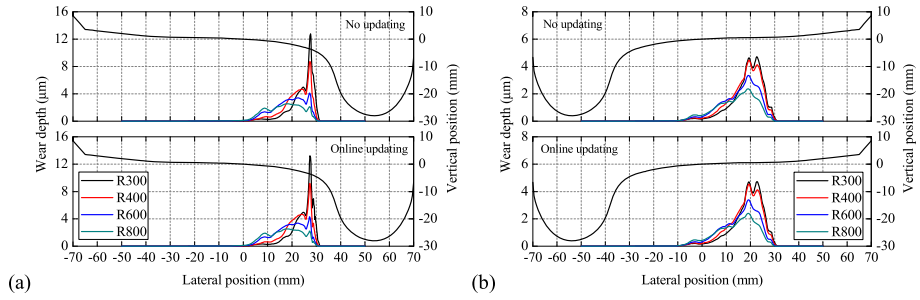
Fig. 15 Comparison between the flexible and rigid track models based on the leading wheelset wear depths on curved tracks with large radii: (**a**) outer wheel and (**b**) inner wheel


Fig. 16 Comparison between the flexible and rigid track models based on the wheel wear area: (**a**) first wheelset, (**b**) second wheelset, (**c**) third wheelset, and (**d**) fourth wheelset

depths for the two models are different. In the flexible model, the track vibration is taken into account, and it is closer to the actual situation.

To further compare the differences in the wheel wear predicted by the flexible and rigid track models, the wear area is derived. The wear area is the region formed by the wear spreading and the lateral axis. It can be obtained by integrating the wear depth at each lateral position. Figure 16 shows the wear area of each wheel calculated with the flexible and rigid track models. It can be found that the difference is relatively small for the leading wheelset of each bogie, except for the outer wheel on R300 and R400 curved tracks. The wear areas for the rigid track model are 6.24% and 2.69% larger than those for the flexible track model

Fig. 17 Comparison of the leading wheelset wear depths on the curved tracks with small radii without and with online updating: (**a**) outer wheel and (**b**) inner wheel
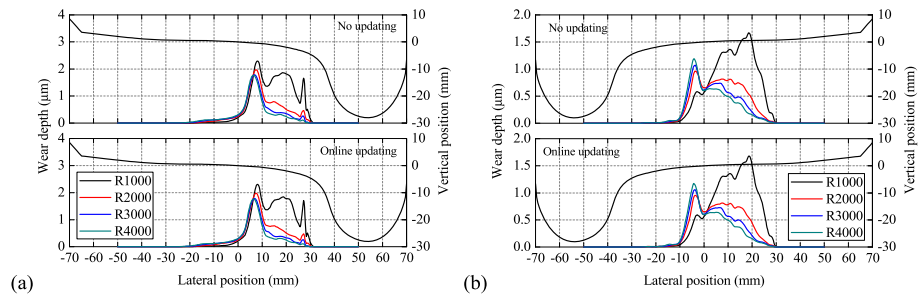
Fig. 18 Comparison of the leading wheelset wear depths on the curved tracks with large radii without and with online updating: (**a**) outer wheel and (**b**) inner wheel

for the outer wheel on R300 and R400 curved tracks, respectively. The differences in the trailing wheelset are more obvious than that of the leading wheelset. The wear area for the rigid track model is larger than that for the flexible track model for each curved track. The average increase is 4.5%.

3.3 Effects of the updating strategy on wheel wear

Two wheel profile updating strategies are considered in this paper. The first is that the wheel profiles remain constant during the dynamic simulation, and the second one is that the wheel profiles are updated per revolution. The simulation cases are the same as the previous section. Figures 17 and 18 compare the wear spreading of the leading wheelset on the curved tracks with small and large radii, respectively. The wear spreading for the two updating strategies is almost the same, and the wear area of each wheel also has a minor difference, as shown in Fig. 19. The simulation results indicate that the strategy of keeping the wheel profiles unchanged during the dynamic simulation coincides with the online updating strategy in terms of the predicted wear.

4 Conclusions

A new online prediction model for wheel wear considering the track flexibility is developed in this study. The model consists of two parts that interact with each other, namely,
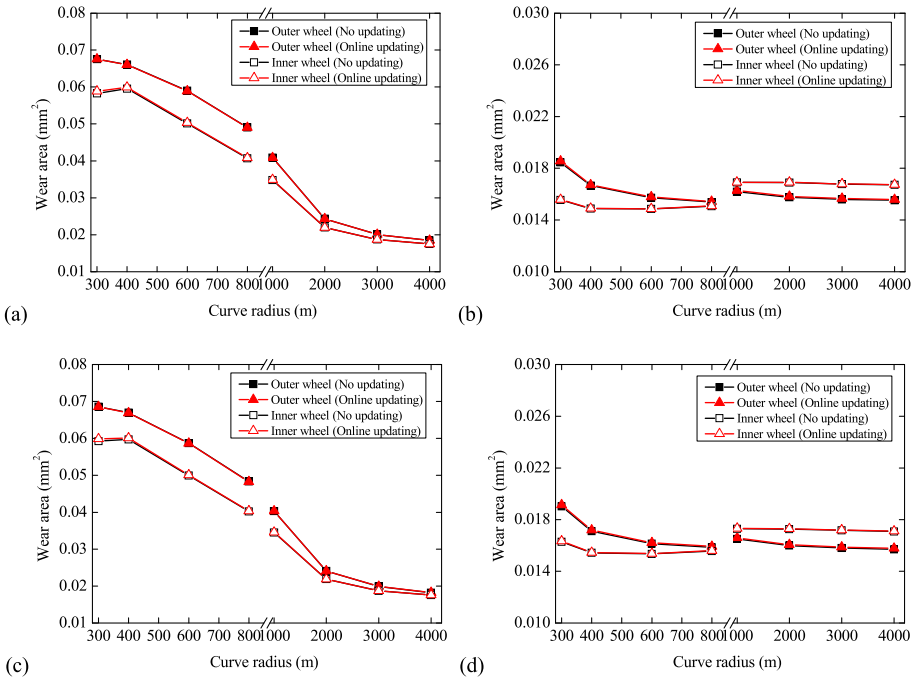
Fig. 19 Comparison of wheel wear area without and with online updating: (**a**) first wheelset, (**b**) second wheelset, (**c**) third wheelset, and (**d**) fourth wheelset

(a) a locomotive/track coupled dynamics model considering the track flexibility, which is validated by the field measurement results, and (b) a model for the wear estimation. Based on the vertical and lateral vehicle/track coupled dynamics theory, a 3D dynamics model of a locomotive coupled with a ballasted track is developed. The coupled locomotive/track dynamics model includes three subsystems: the locomotive, track, and wheel–rail contact. The locomotive subsystem is modeled based on a multi-body dynamic theory. The flexibility of all the components of the locomotive is ignored, but the track flexibility is considered in the current model. The rails are modeled as Timoshenko beams discretely supported by sleepers. Each sleeper is assumed to be a lumped mass, and the lateral, vertical, and roll motions are considered. The ballast bed is considered equivalent to rigid ballast bodies. Only the vertical motion of the ballast bed is considered. The normal and tangential wheel/rail contact forces are calculated with the Hertzian theory and simplified theory of Kalker applied in FASTSIM, respectively. The USFD wear function considering the energy dissipated in the wheel/rail contact patch with a worn material is used to estimate the wheel wear. The wheel wear prediction model can be employed in online solutions instead of in post-processing. The effect of the track flexibility on the wear estimation is analyzed, and the results are compared with those obtained from a rigid track. Moreover, the effect of the wheel profile updating strategy on the wheel wear is also investigated. The simulation results indicate that the track flexibility cannot be neglected for the wheel wear prediction. The wear predicted with the rigid track model is generally larger than that predicted with the flexible track model. However, the strategy of keeping the wheel profiles unchanged during the dynamic simulation coincides with the online updating strategy in terms of the predicted wear.

Publisher's Note   Springer Nature remains neutral with regard to jurisdictional claims in published maps and institutional affiliations.

References

1. Jendel, T.: Prediction of wheel profile wear—comparisons with field measurements. Wear **253**(1–2), 89–99 (2002)
2. Braghin, F., Lewis, R., Dwyer-Joyce, R.S., Bruni, S.: A mathematical model to predict railway wheel profile evolution due to wear. Wear **261**(11–12), 1253–1264 (2006)
3. Lewis, R., Dwyer-Joyce, R.: Wear mechanisms and transitions in railway wheel steels. Proc. Inst. Mech. Eng., Part J J. Eng. Tribol. **218**(6), 467–478 (2004)
4. Lewis, R., Dwyer-Joyce, R., Olofsson, U., Pombo, J., Ambrósio, J., Pereira, M., Ariaudo, C., Kuka, N.: Mapping railway wheel material wear mechanisms and transitions. Proc. Inst. Mech. Eng., Part F J. Rail Rapid Transit **224**(3), 125–137 (2010)
5. Ding, J., Li, F., Huang, Y., Sun, S., Zhang, L.: Application of the semi-Hertzian method to the prediction of wheel wear in heavy haul freight car. Wear **314**(1–2), 104–110 (2014)
6. Ayasse, J.B., Chollet, H.: Determination of the wheel rail contact patch in semi-Hertzian conditions. Veh. Syst. Dyn. **43**(3), 161–172 (2005)
7. Zobory, I.: Prediction of wheel/rail profile wear. Veh. Syst. Dyn. **28**, 221–259 (1997)
8. Ignesti, M., Marini, L., Meli, E., Rindi, A.: Development of a model for the prediction of wheel and rail wear in the railway field. J. Comput. Nonlinear Dyn. **7**(4), 1–14 (2012)
9. Auciello, J., Ignesti, M., Malvezzi, M., Meli, E., Rindi, A.: Development and validation of a wear model for the analysis of the wheel profile evolution in railway vehicles. Veh. Syst. Dyn. **50**(11), 1707–1734 (2012)
10. Ignesti, M., Malvezzi, M., Marini, L., Meli, E., Rindi, A.: Development of a wear model for the prediction of wheel and rail profile evolution in railway systems. Wear **284–285**, 1–17 (2012)
11. Ignesti, M., Innocenti, A., Marini, L., Meli, E., Rindi, A.: Development of a model for the simultaneous analysis of wheel and rail wear in railway systems. Multibody Syst. Dyn. **31**(2), 191–240 (2014)
12. Innocenti, A., Marini, L., Meli, E., Pallini, G., Rindi, A.: Prediction of wheel and rail profile wear on complex railway networks. Int. J. Rail Transp. **2**(2), 111–145 (2014)
13. Shen, Z.Y., Hedrick, J.K., Elkins, J.A.: A comparison of alternative creep force models for rail vehicle dynamic analysis. In: Proceedings of 8th IAVSD Symposium, pp. 591–605. MIT, Cambridge (1983)
14. Kalker, J.J.: A fast algorithm for the simplified theory of rolling contact. Veh. Syst. Dyn. **11**, 1–13 (1982)
15. Pombo, J., Ambrósio, J., Pereira, M., Lewis, R., Dwyer-Joyce, R., Ariaudo, C., Kuka, N.: A study on wear evaluation of railway wheels based on multibody dynamics and wear computation. Multibody Syst. Dyn. **24**, 347–366 (2010)
16. Vollebregt, E.A.H., Iwnicki, S.D., Xie, G., Shackleton, P.: Assessing the accuracy of different simplified frictional rolling contact algorithms. Veh. Syst. Dyn. **50**(1), 1–17 (2012)
17. Zhang, J., Xu, B., Guan, X.: A combined simulation procedure for wear assessment of the HXN5 locomotive. Wear **314**, 305–313 (2014)
18. Li, X., Jin, X., Wen, Z.F., Cui, D., Zhang, W.: A new integrated model to predict wheel profile evolution due to wear. Wear **271**(1–2), 227–237 (2011)
19. Jin, X., Wen, Z., Zhang, W., Shen, Z.: Numerical simulation of rail corrugation on curved track. Comput. Struct. **83**, 2052–2065 (2005)
20. Jin, X., Wen, Z., Xiao, X., Zhou, Z.: A numerical method for prediction of curved rail wear. Multibody Syst. Dyn. **18**, 531–557 (2007)
21. Aceituno, J.F., Wang, P., Wang, L., Shabana, A.A.: Influence of rail flexibility in a wheel/rail wear prediction model. Proc. Inst. Mech. Eng., Part F J. Rail Rapid Transit **231**(1), 57–74 (2017)
22. Jin, X., Wu, P., Wen, Z.: Effects of structure elastic deformations of wheelset and track on creep forces and wheel/rail rolling contact. Wear **253**(1–2), 247–256 (2002)

23. Zhai, W., Wang, K., Cai, C.: Fundamentals of vehicle-track coupled dynamics. Veh. Syst. Dyn. **26**(1), 61–79 (2009)
24. Gialleonardo, E., Di Braghin, F., Bruni, S.: The influence of track modelling options on the simulation of rail vehicle dynamics. J. Sound Vib. **331**(19), 4246–4258 (2012)
25. Tian, Y., Liu, S., Daniel, W.J.T., Meehan, P.A.: Investigation of the impact of locomotive creep control on wear under changing contact conditions. Veh. Syst. Dyn. **53**(5), 692–709 (2015)
26. Tian, Y., Daniel, W.J.T., Meehan, P.A.: Real-time rail–wheel wear damage control. Int. J. Rail Transp. **4**(2), 113–129 (2016)
27. Arias-Cuevas, O., Li, Z., Popovici, R.I., Schipper, D.J.: Simulation of curving behaviour under high traction in lubricated wheel–rail contacts. Veh. Syst. Dyn. **48**(Suppl.), 299–316 (2010)
28. Zhai, W.M., Cai, C.B., Guo, S.Z.: Coupling model of vertical and lateral vehicle/track interactions. Veh. Syst. Dyn. **26**(1), 61–79 (1996)
29. Liang, L., Xiao, X.B., Xiong, J.Y., Zhou, L., Wen, Z.F., Jin, X.S.: A 3D model for coupling dynamics analysis of high-speed train/track system. J. Zhejiang Univ. Sci. A, Appl. Phys. Eng. **15**(12), 964–983 (2014)
30. Timoshenko, S.: Vibration Problems in Engineering, 4th edn. Wiley, USA (1974)
31. Xiao, X., Jin, X., Wen, Z., Zhu, M., Zhang, W.: Effect of tangent track buckle on vehicle derailment. Multibody Syst. Dyn. **25**(1), 1–41 (2011)
32. Zhai, W.M.: Two simple fast integration methods for large-scale dynamic problems in engineering. Int. J. Numer. Methods Eng. **39**(24), 4199–4214 (1996)
33. Zhai, W.M.: Vehicle-Track Coupling Dynamics, 3rd edn. Science, Beijing (2007) (in Chinese)
34. Enblom, R., Berg, M.: Simulation of railway wheel profile development due to wear—influence of disc braking and contact environment. Wear **258**, 1055–1063 (2005)
35. GB/T 5599-85: Railway vehicles—specification for evaluation the dynamic performance and accreditation test. Standardization Administration of the People's Republic of China (1985) (in Chinese)
36. Office for research and experiments, method for assessing riding quality of vehicle. Report C116/RP8, Utrecht, The Netherlands (1977)